



Development of a multi-element ablation strategy enhanced by neural networks to compute graphite ablation during atmospheric entry

Vivien Loridan, Gabriel Prigent, Fabien Chopin, Simon Peluchon

Abstract

In the context of atmospheric entry, a numerical platform that couples a computational fluid dynamics module and a material thermal response solver has been developed over the last decades and has been enriched over time with different ablation strategies, such as the historical ablation model that relies on B' tabulation, or more recently the nonequilibrium multi-species ablation approach. The purpose of this work is to focus on a third strategy: the multi-element ablation model. It aims at taking the advantages from both the aforementionned frameworks, as it is shown to be more predictive than the usual B' tabulations and to be more computationally competitive than the exhaustive multi-species ablation paradigm. For this new formulation, the Navier-Stokes equations have been rewritten in terms of chemical elements, allowing to deal with a reduced number of chemical entities (i.e. only the atomic components of the chemical species) and thus shrinking the size of the whole Navier-Stokes system to solve. Under the assumption of chemical equilibrium, the proportions of chemical species that govern the flow properties are retrieved at each iterative step by using the equilibrium solver of the open-source Mutation++ library. Computing efficiency has additionally be gained by replacing the successive calls to Mutation++ with a neural network that has been trained to emulate its behavior. As a validating framework, 2D axisymmetric simulations are carried out on three different configurations. The first two rely on the arc-jet tests conducted respectively in the VKI's Plasmatron facility and in the Interactive Heating Facility at NASA Ames Research Center, and the third one is related to the atmospheric entry of the IRV-2 vehicle. The multi-element approach using the solver from Mutation++ is shown to be reliable and efficient compared with its multi-species counterpart. With the use of the neural network, the results remain accurate with a gain in computational time up to a factor of 4.

Keywords: aerothermodynamics, ablation, multi-element

Nomenclature

LatinGreekc – Species mass fraction ϵ – Internal energy \tilde{c} – Element mass fraction κ – Conductivity μ – Viscosity \dot{m} – Mass flow rate E – Total energy ρ – Density p - Pressure t - Time Subscriptsi - Species T – Temperature k - Element $\tau_{xx}, \, \tau_{xy}, \, \tau_{yy}$ – Viscous stress components F - Fluid property u, v - Velocity components S – Solid property

¹ CEA-Cesta, 15 avenue des Sablières − CS 60001, 33116 Le Barp Cedex, vivien.loridan@cea.fr

²CEA-Cesta, 15 avenue des Sablières – CS 60001, 33116 Le Barp Cedex, gabriel.prigent@cea.fr

³CEA-Cesta, 15 avenue des Sablières – CS 60001, 33116 Le Barp Cedex, fabien.chopin@cea.fr

⁴CEA-Cesta, 15 avenue des Sablières – CS 60001, 33116 Le Barp Cedex, simon peluchon@cea.fr

1. Contextualization

During atmospheric entry, the high heat fluxes imposed on the heat shield of a hypersonic spacecraft can challenge the integrity of its payload. To prevent such potential damages, the vehicle is typically equipped with a thermal protection system (TPS) that is designed to absorb an important part of the incoming energy via its gradual degradation during the entire reentry phase. To control such ablation phenomenon, it is necessary to better understand the complex interactions between the flow and the vehicle occurring at the gas-solid interface. In this context, a numerical platform that couples a computational fluid dynamics (CFD) module and a material thermal response (MTR) solver has been developed over the last 10 years and has been enriched over time with different ablation strategies.

The first implemented ablation paradigm is based on the B' tabulation, which has been historically used to assess the blowing rate of the recessing wall in the framework of a single gas (air) at chemical equilibrium [1, 2]. Although such strategy has proven its reliability and efficiency over the past few decades, it suffers from many assumptions that are prone to be broken when applied to realistic descent trajectories. Such hypotheses include the consideration of a chemical equilibrium, no injection of the ablated carbonaceous species into the flow and the use of convective coefficients that directly depend on the boundary layer location.

To overcome these aforementioned limitations, several developments have emerged in CFD codes with adapted multi-species ablation models to tackle nonequilibrium surface chemistry. For example, [3, 4] performed simulations of hypersonic reacting flows including thermochemical nonequilibrium effects at a few selected points taken respectively from the trajectory of the Stardust and the IRV-2 reentry vehicles. They took advantage of the strongly coupled LeMANS and MOPAR codes to reproduce the complex interactions between the flow and the heatshield. It is also worth to mention the recent development of the US3D numerical platform, which is designed to be the next generation version of the DPLR code, through a collaboration between the University of Minnesota and the NASA Ames Research Center [5]. Finally, [6] developed a Near Body Solver (NBS) integrated into an off-body block-stuctured Cartesian Higher-Order Adaptive Multi-Physics Solver (CHAMPS) that relies on Immersed Boundary Method (IBM). Such so-called CHAMP NBS-Cart solver for aerodynamics has been coupled to a material response solver, KATS-MR (Kentucky Aerothermodynamics and Thermal Response System), to perform graphite ablation with nonequilibrium chemistry [7]. Regarding these interesting milestones, a more relevant nonequilibrium multi-species ablation model has recently been proposed and implemented within the aerothermal inhouse code [8]. It enables to take account of the carbonaceous species expelled from the wall due to chemical erosion within the flow resolution. Despite its acknowledged ability to properly predict ablation under high-enthalpy flow conditions, this second multi-species method however requires a significant increase of computational time and resources and is consequently not yet fully adapted to routine simulations.

In order to alleviate such necessary computing memory, while being still more predictive than the usual B' tabulations, a third strategy - the so-called multi-element ablation model - has lately been developed and tested within coupled fluid / thermal computations. For such formulation, the Navier-Stokes equations have been rewritten in terms of chemical elements, allowing to deal with a reduced number of chemical entities (i.e. only the atomic components of the chemical species) and thus shrinking the size of the whole Navier-Stokes system to solve. Under the assumption of chemical equilibrium, the corresponding proportions of chemical species that govern the flow properties are retrieved at each iterative step by using the equilibrium solver of the open-source Mutation++ library [9]. Computing efficiency can additionally be gained by replacing the successive calls to Mutation++ with a dedicated neural network that has been trained to emulate the behavior of the aforementioned equilibrium solver [10].

The present work is organized as follows. First, the aerothermal coupling approach as well as the multielement ablation model are described. The second and third parts present 2D-axisymmetric simulations respectively related to two arcjet experiments (VKI and NASA ARC) and to a realistic reentry trajectory (IRV-2 vehicle). It aims at confirming the reliability and efficiency of the multi-element ablation model to predict complex gas-solid interactions at stake during atmospheric entry. The last part finally emphasizes the integration of neural networks within the multi-element strategy to optimize and accelerate aerothermal computations.

2. Aerothermal coupling

The aerothermal code used in this study includes a Navier-Stokes solver (CFD) and a heat conduction module for the material (MTR) that are strongly coupled and embedded in the same numerical platform.

2.1. Navier-Stokes solver

2.1.1. General multi-species formulation

The CFD solver currently developed at CEA-CESTA solves 2D-planar, 2D-axisymmetric and 3D Navier-Stokes equations for flows in chemical equilibrium (the surrounding air being treated as a single species) or nonequilibrium (multi-species reacting flows). Thermal equilibrium (single temperature) is nevertheless assumed in the present study.

The conservation equations at stake can commonly be written under the following differential form

$$\begin{cases} \frac{\partial \rho_i}{\partial t} + \boldsymbol{\nabla} \cdot (\rho_i \boldsymbol{v} + \boldsymbol{J}_i) = \dot{\omega}_i, \\ \frac{\partial \rho \boldsymbol{v}}{\partial t} + \boldsymbol{\nabla} \cdot (\rho \boldsymbol{v} \otimes \boldsymbol{v} + p\underline{I} - \underline{\tau}) = 0, \\ \frac{\partial \rho E}{\partial t} + \boldsymbol{\nabla} \cdot \left(\rho H \boldsymbol{v} + \boldsymbol{q} + \sum_i \boldsymbol{J}_i h_i - \underline{\tau} \boldsymbol{v}\right) = 0, \end{cases}$$

for which ρ_i is the density of species i ($i=1,...,n_s$ with n_s being the total number of chemical species), ρ is the total gas density, \boldsymbol{v} is the bulk velocity field, E is the total energy, p being the pressure, $\underline{\tau}$ the shear stress tensor and $H = E + p/\rho$ the total enthalpy. The source term $\dot{\omega}_i$ governs the gain or loss of species i through chemical reactions. The viscous stress tensor is related to a Newtonian fluid via

$$\underline{\underline{\tau}} = \mu \, \left[\left(\boldsymbol{\nabla} \otimes \boldsymbol{v} \right) + \left(\boldsymbol{\nabla} \otimes \boldsymbol{v} \right)^\top \right] + \lambda \, \left(\boldsymbol{\nabla} \cdot \boldsymbol{v} \right) \, \underline{\underline{I}}.$$

In the above formulations, $\lambda = -2/3 \,\mu$ according to Stokes' hypothesis. The mixture viscosity μ is obtained via Wilke's semi-empirical mixing rule [11] with species viscosities calculated using Blottner's model [12]. Heat fluxes involved in the energy conservation equation are modeled according to Fourier's law

$$q = -\kappa \nabla T + \sum_{i} J_{i} h_{i},$$

including the contribution of thermal conduction and diffusion. The mixture conductivity κ is obtained using Prandtl's relation $\kappa = \mu C_p/P_r$ with Prandtl number $P_r = 0.67$. Mass fluxes are modeled according to Fick's law

$$\boldsymbol{J}_i = -\rho D_i \boldsymbol{\nabla} c_i,$$

for which c_i is the mass fraction of species i and D_i is the (diagonal) diffusion coefficient related to species i. The diffusivity model for each species is given by the Lewis model $\rho D = \kappa L_e/C_p$ for which C_p is the specific heat at constant pressure. In what follows, the Lewis number is set to $L_e = 1.4$.

Numerically, the code employs multi-block structured grids on a body-fitted coordinate system. A finite-volume formulation is used for the inviscid fluxes, which are typically discretized according to a modified version of the Roe scheme that turned out to be particularly adapted for shock capturing (carbuncle-free) and the treatment of multi-species reacting flows. The viscous fluxes are described with a finite-difference paradigm that employs a standard, second-order differencing scheme. The solution of the Navier-Stokes equations is driven to its steady state through an implicit resolution, which requires to calculate the Jacobian matrices related to the inviscid and viscous flux tensors and the source term. Such implicit solver allows aggressive CFL ramping and proved its efficiency in the context of High Performance Computing (HPC).

2.1.2. Derivation of the multi-element framework

For the context of this study, the full Navier-Stokes system has been reformulated in terms of chemical elements with newly derived pseudo transport coefficients and no more chemical source term. The relation between the proportions of chemical species containing chemical element k and the mass fraction \tilde{c}_k of element k is given by

$$\widetilde{c}_k = \sum_i a_i^k \frac{\widetilde{M}_k}{M_i} c_i,$$

for which a_i^k is the number of element k involved in chemical species i. By multiplying the mass conservation equations of the Navier-Stokes system with $\sum_i a_i^k \widetilde{M}_k/M_i$, one obtains the elemental mass conservation equations

$$\frac{\partial \widetilde{\rho}_k}{\partial t} + \boldsymbol{\nabla} \cdot (\widetilde{\rho}_k \boldsymbol{v}) + \boldsymbol{\nabla} \cdot \widetilde{\boldsymbol{J}}_k = 0,$$

with $\widetilde{J}_k = \sum_i a_i^k \widetilde{M}_k / M_i J_i$ and for which the source terms have naturally vanished. For the case of diagonal diffusion $J_i = -\rho D_i \nabla c_i$, the element diffusive mass flux writes

$$\widetilde{\boldsymbol{J}}_{k} = -\sum_{j} \rho \widetilde{D}_{kj} \boldsymbol{\nabla} \widetilde{\boldsymbol{c}}_{j},$$

which is equivalent to deal with multicomponent diffusion with

$$\rho \widetilde{D}_{kj} = \sum_{i} a_{i}^{k} \frac{\widetilde{M}_{k}}{M_{i}} \rho D_{i} \frac{\partial c_{i}}{\partial \widetilde{c}_{j}}.$$

If $\rho D_i = \rho D$ (Lewis), the diffusive mass flux simply reduces to $\tilde{J}_k = -\rho D \nabla \tilde{c}_k$.

During the convergence process of the Navier-Stokes solver, the elemental mass fractions, the total density and the internal energy of the flow are retrieved from the usual conserved quantities calculated by the numerical scheme and are given as inputs to Mutation++ [9]. As output, the open-source library calculates the corresponding species mass fractions, temperature and pressure under the assumption of chemical equilibrium (minimization of the free Gibbs energy). Such procedure is repeated successively at each iterative step of the flow onto every cell of the mesh.

2.2. Material thermal response module

The material thermal response module solves 2D-planar, 2D-axisymmetric and 3D heat conduction in the solid, written under the conservative form as

$$\frac{\partial}{\partial t}(\rho_s h_s) + \boldsymbol{\nabla} \cdot \boldsymbol{q}_s = 0,$$

for which h_s is the enthalpy related to the material and q_s being modeled according to Fourier's law

$$q_s = -\kappa_s \nabla T_s$$
.

Similarly to the flow solver, the energy diffusion equation is solved on a multi-block structured grid. The heat fluxes are discretized via a second-order differencing scheme. The numerical resolution inside the TPS remains implicit, but contrary to the flow resolution, thermal diffusion is unsteady.

2.3. Coupling implementation

2.3.1. Derivation of the general wall boundary conditions

Simulations that are carried out to predict the material ablation of the heat shield of a vehicle during a reentry phase rely on a coupled fluid / thermal approach. From the characteristic timescales related to convection, conduction, diffusion and blowing inside the gas boundary layer, as well as the conducting and ablating effects inside the material, the flow dynamics is, as mentioned earlier, considered steady whereas the heat transport in the TPS is considered unsteady. The coupling rate between the flow and

the material is thus primarily governed by the timescales related to surface recession (ablation). The physical quantities exchanged at the interface between the fluid and the thermal protection system (TPS) are derived from mass and energy balances at the surface at each time step.

To ensure the coupling procedure, relevant surface boundary conditions have to be considered. Their derivation follows the method detailed in [13], for which balance equations used to put forward boundary conditions between two adjoining domains of different natures are established via flux balancing at the interface.

The conservation equations projected on a given cell of width δy that interfaces the fluid and solid gives

$$\delta y \frac{\partial}{\partial t} (\rho c_i) = -\left[\dot{m}c_i + J_{yi}\right]_F + \dot{m}_i + \delta y \,\dot{\omega}_i \tag{1}$$

$$\delta y \frac{\partial}{\partial t} (\rho u) = -\left[\dot{m}u - \tau_{xy}\right]_F + \left[\dot{m}u\right]_S \tag{2}$$

$$\delta y \frac{\partial}{\partial t} (\rho v) = -\left[\dot{m}v + p - \tau_{yy} \right]_F + \left[\dot{m}v + p \right]_S \tag{3}$$

$$\delta y \frac{\partial}{\partial t} (\rho E) = -\left[\dot{m}H - \tau_{xy}u - \tau_{yy}v + q_y\right]_F + \left[\dot{m}H + q_y\right]_S \tag{4}$$

respectively for mass, momentum and energy balance. The mass balance equation (1) adapted to the multi-element strategy reduces to

$$\delta y \, \frac{\partial}{\partial t} \left(\rho \widetilde{c}_k \right) = - \left[\dot{m} \widetilde{c}_k + \widetilde{J}_{yk} \right]_F + \widetilde{\dot{m}}_k$$

with

$$\widetilde{\dot{m}}_k = \sum_i a_i^k \, \frac{\widetilde{M}_k}{M_i} \dot{m}_i.$$

Since the wall recession rate v_w is less smaller than the blown flow velocity v at the wall, the momentum conservation equations (2) and (3) reduce, at steady state, to $p_S = p + \dot{m}v - \tau_{yy}$, which in practice is equivalent to $p_S = p_F$. From equation (4), the simplified surface energy balance equation (steady state ablation) used to relate the conductive heat flux $[q_y]_S$ with the wall convective flux $[q_y]_F$ is written as

$$[q_y]_S = [q_y]_F - \dot{m} (H_S - H_F).$$

Exhibiting the energy balance equation into this specific formulation simply illustrates that the energy absorbed by the removal of material from the surface is not used to heat the TPS, thus keeping the vehicle wall at a relatively moderate temperature.

2.3.2. Coupling procedure

The coupling procedure for a multi-species nonequilibrium flow or a multi-element equilibrium flow is performed as follows. First, the surface mass balance (SMB) equation is solved, enabling to deduce the ablation mass flow rate, as well as the mass fraction of the species (or elements) at the wall expelled into the flow from the degradation of the heat shield. The latter are considered as boundary conditions for the Navier-Stokes system of equations, which is solved by the CFD module towards its steady state. The surface energy balance (SEB) equation is then considered to relate the heat flux conducted from the surface into the solid with the convective wall heat flux that has been calculated during the aforementioned hydrodynamic step. Such thermal conductive flux serves as a boundary condition for the time-dependent material response module that specifically computes the heat conduction into the vehicle. Once the heat transfer equation is solved inside the TPS, a new surface temperature is deduced, which is used as a wall boundary condition for the next time-step of the coupled fluid / solid iterative process. The total mass flow rate \dot{m} obtained after each computational loop enables to calculate the wall recession rate v_w via the relation $v_w = \dot{m}/\rho_s$ (ρ_s being the density of the solid). The corresponding mesh displacement is therefore derived to adjust the shape of the vehicle in accordance with the ablation rate.

With such algorithm, the thermal response code is directly integrated as a boundary condition of the Navier-Stokes solver, thus taking advantage of the implicit nature of the code as well as the aggressive CFL ramping.

3. Validation of the multi-element ablation model

The advantages and limitations of the multi-element ablation strategy are first investigated through two different experimental test-cases. The results are compared with the provided data as well as with the simulations obtained from the multi-species ablation model.

For the computations presented below, the chemistry model consists of 11 species, namely N_2 , O_2 , NO, N and O to describe nonionizing air, as well as CO_2 , CO, CN, C, C_2 , C_3 , which come from gassurface interactions and are fully part of the flowfield. For the nonequilibrium multi-species strategy, the gas-phase chemical kinetics model is based on [14, 15], which take account of dissociation and neutral exchange. As mentionned above, all the chemical species are assumed to diffuse at the same velocity (Lewis model for diffusion).

The finite-rate surface chemistry model (heterogeneous chemistry) considered to compute the mass flow rate includes carbon oxidation, nitridation and sublimation. Because non general common opinion exists between the large variety of well-established finite-rate surface chemistry models [16, 17], several oxidation [14, 18–23] and nitridation [14, 19–21, 23] models have been implemented and tested. Carbon sublimation is governed by a Knudsen-Langmuir formulation for nonequilibrium surface evaporation as depicted in [24].

3.1. VKI test case

3.1.1. Presentation of the VKI test case

The first test-case is an experimental campaign that has been conducted in VKI's Plasmatron facility. It consists of a hemispherical graphite sample with a radius of 2.5 cm, extended by 1.5 cm and immersed in an air plasma torch in subsonic conditions during 640 seconds. The stream enthalpy is estimated to be approximately 25.7 MJ/kg, with an obtained stagnation point pressure of 0.10 atm and a stagnation point cold-wall heat flux of 1.44 MW/m². High-quality data regarding the sample's recession and surface temperature over time are provided in [25].

The mesh used to obtain axisymmetric solutions of the flow around the graphite sample contains 130 cells in the axial direction and 62 cells along the body, on a grid moving with the recessing surface. The upstream flow conditions have been pre-computed to match the experimental conditions prescribed above for a flow at chemical equilibrium by using the torch's flow rate and the dimensions of the facility [26]. They are summarized in Table 1.

Parameter	Value for equilibrium
Velocity	$232 \mathrm{m/s}$
Temperature	$6210~\mathrm{K}$
Pressure	10^4 Pa
c_{O_2}	0.00209
$c_{ m N_2}$	0.36520
$c_{ m NO}$	0.00001
$c_{ m N}$	0.40090
$c_{ m O}$	0.23180

Table 1. Freestream conditions for the VKI test-case

3.1.2. Numerical results

For the present test-case, two computations have been performed, first with the classical multi-species ablation model and secondly with the multi-element ablation strategy, both using the so-called Air-

Carbon Ablation (ACA) oxidation and nitridation models from [23]. The time evolution of surface recession and species mass fractions are presented in Figure 1. It appears that both simulations provide similar results in terms of surface recession. Such correspondence confirms the validity of the chemical equilibrium assumption and is a first evidence of the reliability of the multi-element strategy for such scenario. Because the surface temperature does not exceed 2500 K, graphite ablation is only due to oxidation with no sublimation (absence of C_3 for example). Noticeable differences remain between both models on the species mass fraction at stagnation point, specifically on the proportions of CO_3 and CO_4 , the latter being preferentially produced with the equilibrium multi-element paradigm. In terms of computing performance, the simulations related to the multi-element ablation model runs about 5 times faster than the multi-species counterpart.

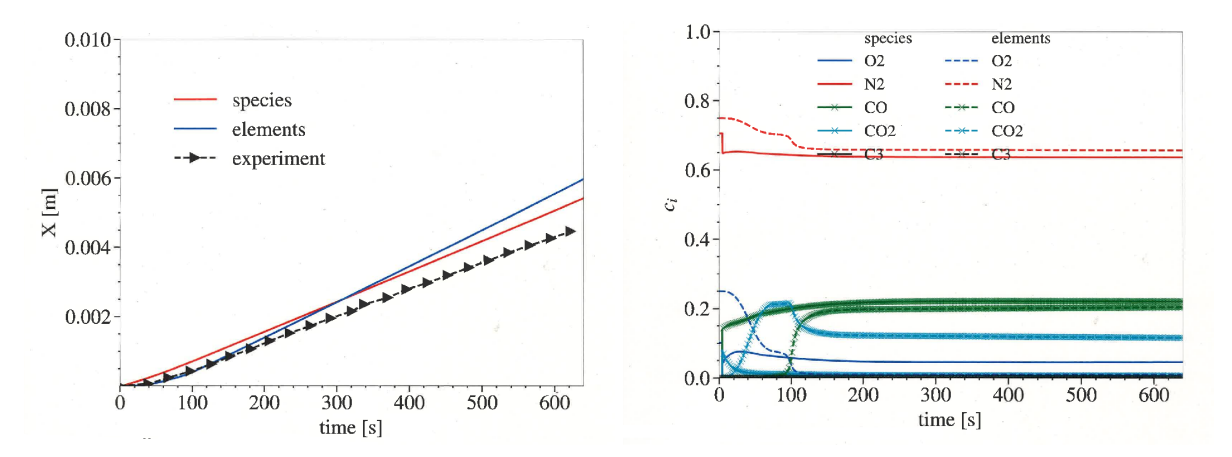


Fig 1. Surface recession at stagnation point vs time (left) and species mass fractions at stagnation point vs time (right). Surface recession is shown in red when computed with the multi-species ablation model and in blue for the multi-element ablation model. Experimental data are shown in black (triangles). Species mass fractions are in plain lines when computed with the multi-species ablation model and in dotted lines for the multi-element ablation model.

The results correctly reproduce the experimental data despite a slight overestimation of the provided surface recession. Such discrepancy might be due to the deviations inferred in the reconstruction of the inflow conditions. A dedicated reconstruction of the inflow conditions at chemical nonequilibrium should be tested in the future. The influence of other carbon oxidation models can also be investigated.

3.2. IHF test case

3.2.1. Presentation of the IHF test case

Another well-referred test case consists of the interaction between a graphite sphere cone and a high-enthalpy arc-jet stream during 30 seconds. Such experimental campaign has been conducted in the Interactive Heating Facility (IHF) at NASA Ames Research Center (ARC) [27]. The graphite model is a 10 deg half-angle sphere cone with nose radius of 1.905 cm and total length of 8.89 cm. The stream enthalpy is estimated to be approximately $27 \,\mathrm{MJ/kg}$, with an obtained stagnation point pressure of 0.75 atm and a stagnation point cold-wall heat flux of $21 \,\mathrm{MW/m^2}$. Such experimental case has been studied in various works [7, 28–30].

In the present study, the mesh used to obtain axisymmetric solutions of the flow around the graphite sample contains 100 cells in the axial direction and 100 cells along the body, on a grid moving with the recessing surface. The upstream flow conditions are summarized in Table 2. They have been established to match the experimental conditions prescribed above and described in [27], either for a flow at chemical equilibrium [30] or chemical nonequilibrium [28] (partially dissociated air flow). The oxidation model used for the computations are taken from [18] with no nitridation, as it has been shown to reproduce remarkably well the experimental data [8].

Parameter	Value for equilibrium	Value for nonequilibrium
Velocity	7300 m/s	5334 m/s
Temperature	891 K	$1428~\mathrm{K}$
Pressure	379 Pa	1672 Pa
c_{O_2}	0.2300	0.0000
c_{N_2}	0.7700	0.6169
$c_{ m NO}$	0.0000	0.0046
$c_{ m N}$	0.0000	0.1212
$c_{ m O}$	0.0000	0.2573

Table 2. Freestream conditions for the IHF test-case

3.2.2. Numerical results

Figure 2 depicts the evolution of surface recession and species mass fractions at stagnation point during the test (30 seconds) for both the multi-species and multi-element strategies. They are compared with the experimental data when available. The results exhibit significant discrepancies between the nonequilibrium and the equilibrium ablation models, indicating that the flow is likely to be in chemical nonequilibrium. The multi-element strategy predicts the emergence of C_3 coming from the mechanism of sublimation at an early stage of the computation (starting from t=4 seconds), which tends to dramatically increase the ablation rate and thus surface recession. However, for the nonequilibrium ablation model, no C_3 is produced, suggesting that the dominant ablation process that occurs during the whole experiment is likely oxidation.

Let us emphasize the fact that the imposed inflow conditions necessarily have a major impact on the predicted final recession. Because they are very different depending on the considered ablation model (either equilibrium or nonequilibrium), the results differ accordingly.

If the presented multi-element approach cannot be used as such to long-time steady nonequilibrium arcjet experiment, it can however still be convenient for atmospheric entry ballistic trajectories, since the main contribution for ablation occurs at the final stages of the descent (altitudes below 20 km), for which the flow is likely to be at chemical equilibrium.

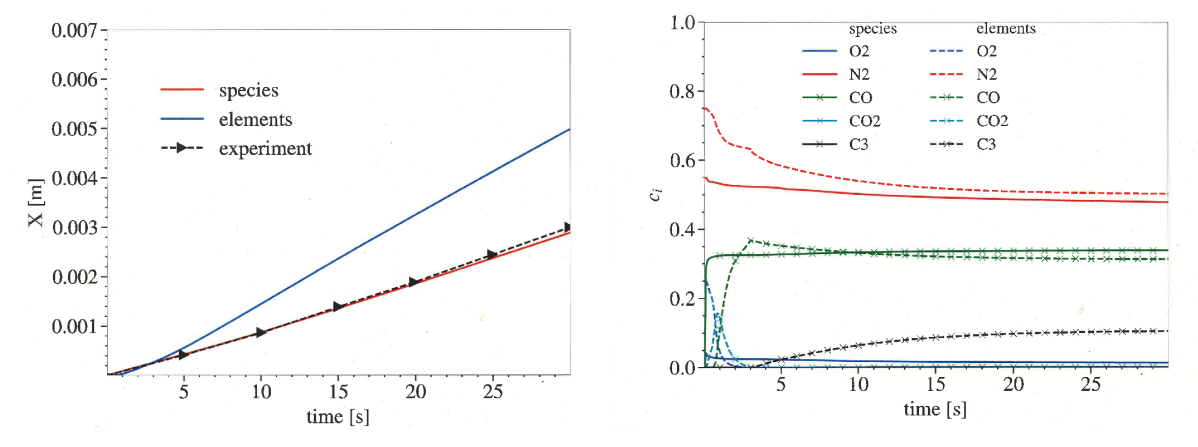


Fig 2. Surface recession at stagnation point vs time (left) and species mass fractions at stagnation point vs time (right). Surface recession is shown in red when computed with the multi-species ablation model and in blue for the multi-element ablation model. Experimental data are shown in black (triangles). Species mass fractions are in plain lines when computed with the multi-species ablation model and in dotted lines for the multi-element ablation model.

4. Reliability of the multi-element strategy for realistic reentry trajectory

4.1. Presentation of the IRV-2 test case

In order to attest the reliability of the multi-element ablation model in a physically more exhaustive background, 2D axisymmetric simulations are carried out on the IRV-2 vehicle, which is also a well-referred test case that employed a TPS composed of non-charring carbon [1, 2, 4, 31]. The IRV-2 vehicle is a sphere-biconic with a nose radius of 0.01905 m and total length of 1.386 m, as shown in Fig. 3.



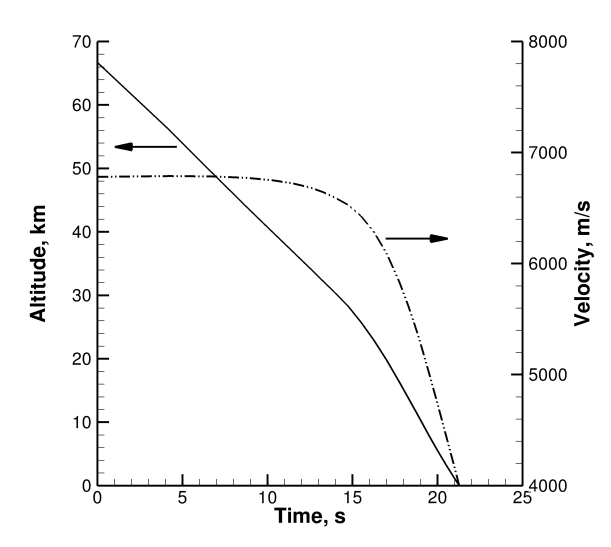


Fig 3. (a) Illustration of the IRV-2 shape. (b) IRV-2 trajectory, depicted by altitude and velocity vs flight time. Source: [4].

The biconic angles are 8.42 and 6.10 deg, respectively, with the break occurring at an axial location of 0.1488 m measured from the stagnation point. For the purpose of corroborating our simulations with previously published results, the freestream conditions considered in the present work are taken from [2], which are illustrated in Fig. 3. Let us point out that such considered trajectory is not exactly the one followed by the IRV-2 vehicle during its actual flight, as the freestream conditions have been artificially re-adjusted in [2] to ensure the stability of their computations.

The present work only focuses on the IRV-2 nosetip (sphere and first cone). The mesh used to obtain axisymmetric solutions of the flow around the forebody of the vehicle contains 250 cells in the axial direction and 88 cells along the body, on a grid moving with the recessing surface. The flow on the nosetip is assumed to be completely laminar during the trajectory. As before, the presented computations are obtained either with the multi-element ablation model and with the more comprehensive multi-species ablation approach presented above.

4.2. Accuracy of the multi-element ablation strategy

Figure 4 illustrates the temperature distribution within the flowfield and inside the material at the end of the trajectory for both the multi-species (top) and the multi-element ablation model (bottom). The results taken from both computations agree well, specifically in terms of final surface recession. Such correlation indicates that most of the material degradation occurring during the flight takes place at the end of the trajectory (low altitudes), for which chemical equilibrium holds.

These claims are confirmed in Figure 5, which represents the evolution of surface recession (left) and species mass fractions (right) at stagnation point with time for both the multi-species and the multi-element strategies. Before t=9 seconds, both recession surfaces are comparable between the multi-species and multi-element models. After 9 seconds, the multi-element model triggers sublimation, as shown by the formation of C_3 , enhancing the mass flow rate and thus increasing the corresponding surface recession compared with the multi-species strategy. The latest predicts sublimation from 13 seconds, which in turns enables to increase the recession rate (slope of the recession surface). It is also

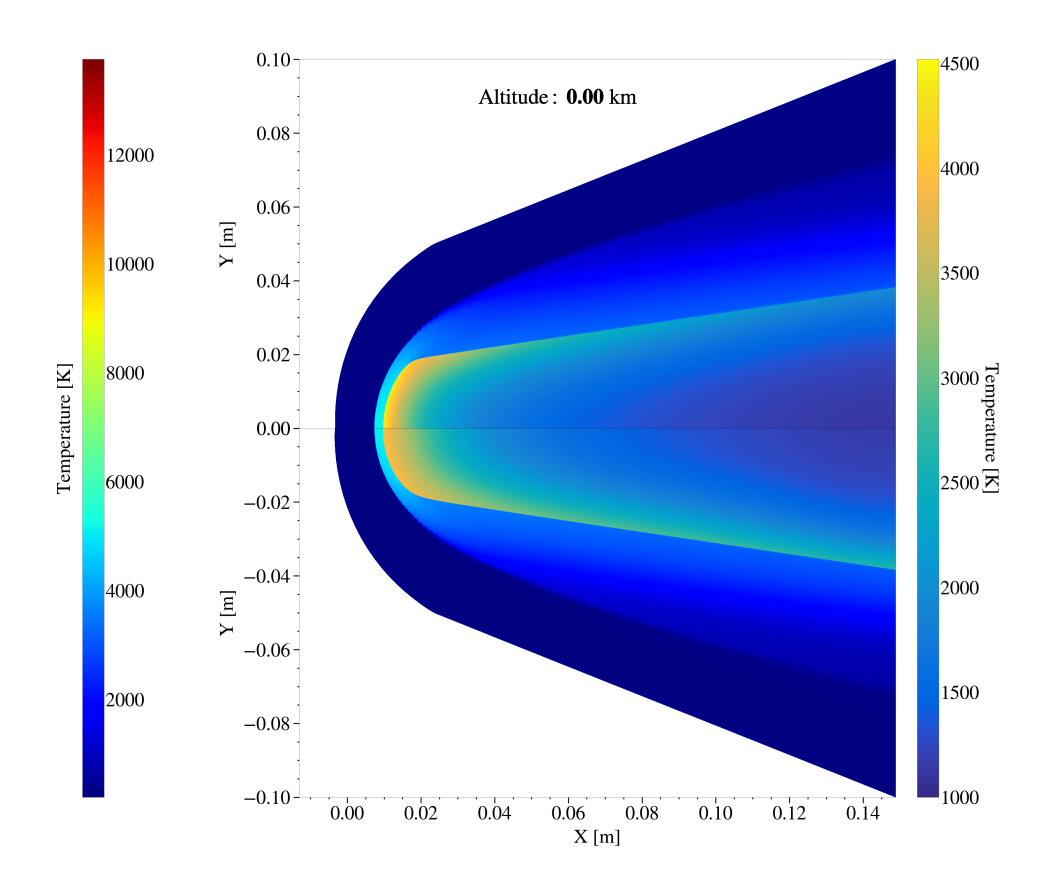


Fig 4. Temperature distribution within the flow and inside the graphite nose of the IRV-2 vehicle at the end of the trajectory (altitude of 0 km) for both the multi-species ablation (top) and the multi-element ablation strategies (bottom).

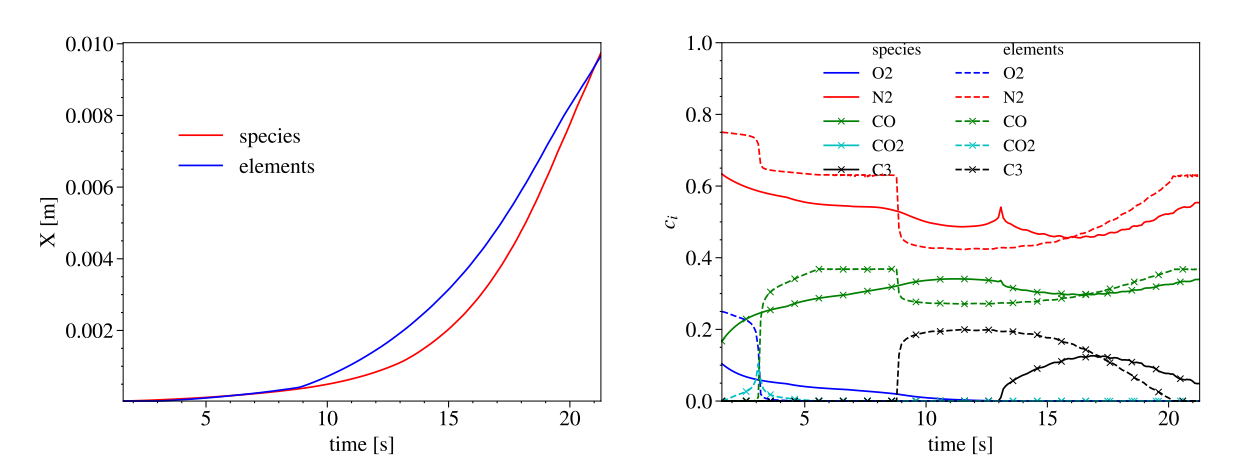


Fig 5. Surface recession at stagnation point vs time (left) and species mass fractions at stagnation point vs time (right). Surface recession is shown in red when computed with the multi-species ablation model and in blue for the multi-element ablation model. Species mass fractions are in plain lines when computed with the multi-species ablation model and in dotted lines for the multi-element ablation model.

important to notice the brief formation of CO_2 at t = 2 seconds when the multi-element model is used, whereas the multi-species model discards the CO_2 production to favor CO.

As before, the computing time is found to be decreased by a factor of 5 when the multi-element model is performed compared with the exhausted nonequilibrium multi-species paradigm. As such, the multi-element model can be used as a cheap - yet still accurate - alternative to aerothermal computations when the flow is closed to chemical equilibrium.

5. Neural networks

To achieve the purpose of further accelerating aerothermal simulations related to the multi-element model, the successive calls to the equilibrium solver from the Mutation++ library can be replaced by a dedicated neural network [10]. Two advantages can be retrieved from this approach. First, contrary to the original multi-element model that has to call the equilibrium solver in each cell of the mesh, neural networks allows to easily vectorize their calls on array-like data structures. Second, because the equilibrium solver is not costly when executed as a standalone application, it is easily possible to build a large training database and substantially improve the neural network's accuracy without additional cost during inference. Given a prescribed set of chemical species, the neural network is thereby applicable, once trained, to any simulation which involves the same chemical species.

Building a dedicated neural network requires the following steps: construct the training database, select hyperparameters and train the network.

5.1. Generation of the dataset

The first step consists in generating a proper database with Mutation++ onto which the neural network is trained and tested. For the aerothermal computations at stakes, only the carbon element is injected due to the ablation of the heat shield (pyrolysis is not considered for the present work), such that in the boundary layer, $\tilde{c}_C \in [0,1]$. Because no additional N or O elements are created, the allowed space for \tilde{c}_N and \tilde{c}_O are such that $\tilde{c}_N \in [\tilde{c}_{N\infty} (1 - \tilde{c}_C) - 0.05, \tilde{c}_{N\infty} (1 - \tilde{c}_C) + 0.05]$ and $\tilde{c}_{O} \in [\tilde{c}_{O\infty} (1 - \tilde{c}_C) - 0.05, \tilde{c}_{N\infty} (1 - \tilde{c}_C) + 0.05]$ ($\tilde{c}_{N\infty}$ and $\tilde{c}_{O\infty}$ are respectively the inflow conditions for N and O), as illustrated in Figure 6. The density ρ and internal energy ϵ are such that $\rho \in [10^{-5}, 10^2]$ kg.m⁻³ and $\epsilon \in [-3.10^5, 3.10^8]$ J.kg⁻¹ in order to cover a wide range of aerothermal frameworks (arcjet experiment or atmospheric entry). In practice, more than 3.10^6 runs of Mutation++ have been performed with random distribution on the aforementioned spaces to generate two databases: the train database and the test database.

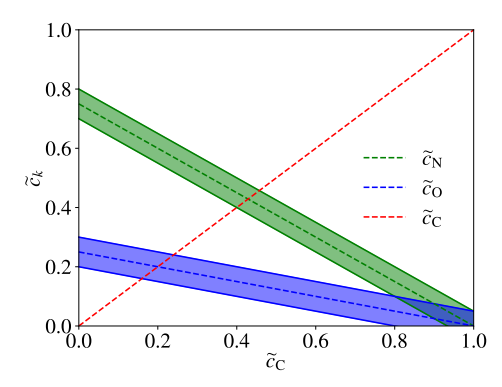


Fig 6. Restricted values for C, N and O elemental mass fractions.

It is indeed necessary to work with these two aforementioned databases. The neural network learns from the training base and is then tested on a second testing base that has not been used by the neural network during its training. Such methodology enables to avoid overfitting, i.e. when the neural network is able to perfectly reproduce the data learnt but is inefficient to match other data that the network has never seen, as illustrated in Figure 7. To guarantee an accurate precision, the data are divided at 80% for the training base and 20% for the testing base.

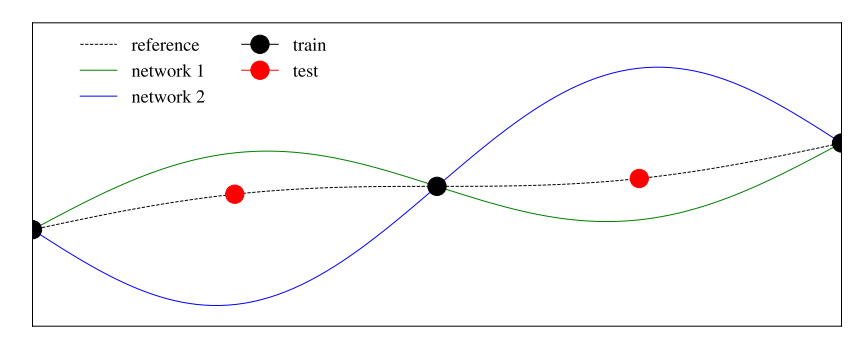


Fig 7. Overfitting issues for two neural networks that have the same accuracy on the training database (black circles). Network 1 (green) remains accurate when applied on the test database (red circles) whereas Network 2 (blue) is inaccurate compared with a reference solution (black dotted line).

5.2. Neural network training and testing

5.2.1. Parameters and Hyper-parameters

The architecture of a neural network, as a machine learning model composed of a succession of layers of interconnected neurons, is mostly defined by the kind of interconnection between the different layers. For the present study, the neural network is a Multi-Layer Perceptron (MLP), also called a Fully-Connected Neural Network, for which each neuron of a layer n is connected to all neurons on the layer n+1.

A MLP is defined by two sets of parameters. The first one, referred as Θ , corresponds to the parameters that will by optimized during the learning process of the network. Among them, let us mention the weight function between layer n and n+1, as well as the bias vector of layer n. The second set of parameters are prescribed and chosen before the training step and describes the shape of the network and its internal architecture. They are usually referred as hyper-parameters, which generally contain the number of layers, the number of neurons per layer, the loss function J, the activation function, the optimizer... For the application at stake, about 20000 neural networks have been trained corresponding to a selection of 20000 hyper-parameters. The accuracy of the neural network depends on all its parameters and hyper-parameters, whereas its computational speed only depends on its number of layers and neurons.

5.2.2. Training methodology

Let us write X the input vector for Mutation++ as $X=(\widetilde{c}_1,\ldots,\widetilde{c}_{ne},\rho,\epsilon)$ and the corresponding outputs $MPP(X)=(c_1,\ldots,c_{ns},P,T)$. The training step consists in looking for a parametric function $(X,\Theta)\to NN(X,\Theta)$ which has to be the closest possible to MPP(X) in a certain metric \mathcal{L} , for example the \mathcal{L}_2 -norm. Such goal is achieved with the optimization of the Θ parameters driven by the minimization of a loss function J such that

$$J(\Theta) = \int (MPP(X) - NN(X, \Theta))^2 dP_X.$$

If the number of training points N is sufficiently large, one can define an approximation $J_N(\Theta)$ of $J(\Theta)$ as

$$J_N(\Theta) = \frac{1}{N} \sum_{i=1}^{N} (MPP(X) - NN(X, \Theta))^2.$$

If the J function is minimized for a set of parameters $\Theta = \Theta^*$, then

$$J(\Theta^*) \le |J_N(\Theta^*) - J_{\text{Test}}(\Theta^*)| + J_{\text{Test}}(\Theta^*) = J_{\text{TS}}(\Theta^*).$$

Convergence is reached when $J_{\rm TS}(\Theta^*)$ is below a given tolerance. Between different produced neural networks, a balance between accuracy and speedup has to be found. Among them, and for the application at stake, a neural network of only 3 layers and 4 neurons per layer with an accuracy of 2.10^{-7} has been chosen.

5.3. Performance analysis on the IRV-2 test case

The case under consideration to test the performance of the neural network is still the IRV-2 vehicle flight, with a specific focus on the last 20 km of the trajectory to ensure the validity of the multi-element ablation approach (chemical equilibrium holds) as discussed above.

Figure 8 represents surface recession (left) and species mass fractions (right) at stagnation point versus time for the the multi-element strategy with Mutation++ and the neural network. The agreement between both computations is very satisfactory, attesting the accuracy of the neural network along a realistic reentry trajectory. The final surface recession matches remarkably well the original (Mutation++) multi-element strategy.

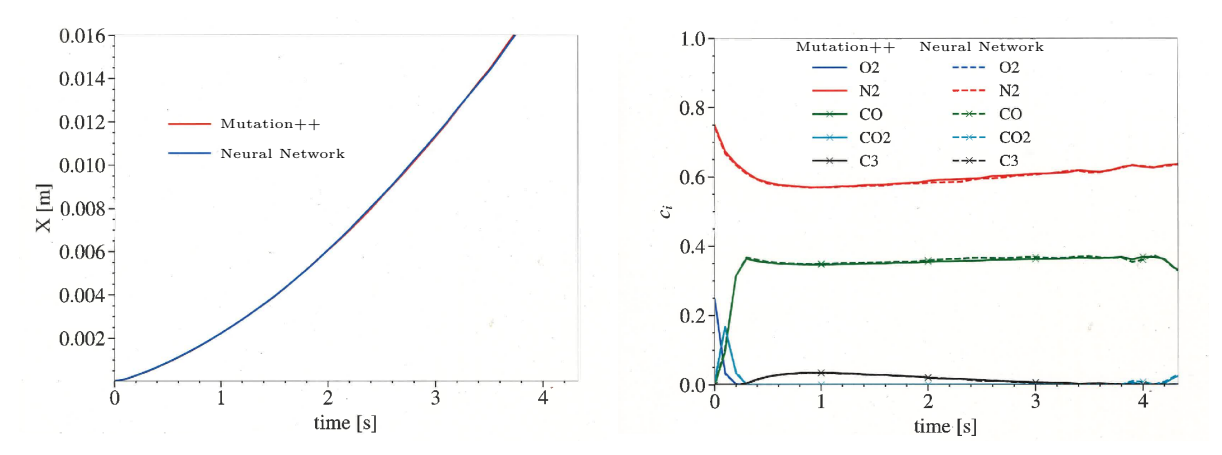


Fig 8. Surface recession at stagnation point vs time (left) and species mass fractions at stagnation point vs time (right). Surface recession is shown in red when computed with the Mutation++ multi-element ablation model and in blue for the multi-element ablation model enhanced by neural networks. Species mass fractions are in plain lines when computed with the Mutation++ multi-element ablation model and in dotted lines for the multi-element model optimized by neural networks.

In terms of computing time, a single call to the neural network is found to be 26 times faster compared with a call to the equilibrium solver from Mutation++, which corresponds to a gain in total computational time of a factor of 4 for the entire simulation. Compared with the classical multi-species ablation model, the multi-element ablation strategy enhanced by neural network is therefore about 20 faster.

5.4. Hybridation

To ensure the exact same accuracy with the neural network as with the use of Mutation++, a short-term perspective would consist in building an optimized hybrid scheme that uses predictions brought by the neural network as an initialization for the Mutation++ scheme, which may hopefully converge in fewer iterations since the first guess is supposed to be close to the convergence state, as depicted in [10]. A first draft has already been implemented in the inhouse aerothermal code, but yet with no noticeable gain in computing time compared with the use of Mutation++ alone. Such strategy still needs to be investigated and optimized in a future work.

6. Conclusions

In the present study, a multi-element ablation model has been described. It can be used as an intermediate approach between the approximate B' ablation method and the exhaustive multi-species nonequilibrium ablation strategy. Its implementation relies on the external equilibrium solver Mutation++, which can be predicted with a dedicated neural network to gain computational efficiency with a reasonable reliability. The results obtained for the presented test-cases suggest that the method can be an accurate alternative method provided the flow does not deviate to much from chemical equilibrium.

More specifically, the computations related to the atmospheric entry of the IRV-2 vehicle show that the heat shield ablation during the entire trajectory can be replicated with the use of the multi-species

ablation model for high altitudes and with the multi-element method for lower altitudes. As a future prospect, one can establish a combined ablation model that enables to switch from the multi-species strategy to the multi-element strategy. Such switch between the two paradigms could be automatically triggered based on the calculations of the chemical timescales at the wall. If the chemical kinetics is orders of magnitude faster than the other flow transport phenomena (convection, diffusion, conduction), chemical equilibrium is relevant and the multi-element ablation model is fully applicable.

As mentioned above, further investigations can be pushed forward to build an optimized hybrid multielement method that uses the neural network as a first guess to help the iterative process of Mutation++to converge faster, with the guarantee of ensuring the exact same accuracy as with the use of the equilibrium solver alone.

Last but not least, the presented model can be easily extended to other pyrolyzing (charring) ablative materials.

References

- [1] Hassan, B., Kuntz, D., and Potter, D., "Coupled Fluid/thermal Prediction of Ablating Hypersonic Vehicles," 36th AIAA Aerospace Sciences Meeting and Exhibit, 1998. https://doi.org/10.2514/6.1998-168.
- [2] Kuntz, D. W., Hassan, B., and Potter, D. L., "Predictions of Ablating Hypersonic Vehicles Using an Iterative Coupled Fluid/Thermal Approach," *Journal of Thermophysics and Heat Transfer*, Vol. 15, No. 2, 2001, pp. 129–139. https://doi.org/10.2514/2.6594.
- [3] Alkandry, H., Boyd, I. D., and Martin, A., "Coupled Flow Field Simulations of Charring Ablators with Nonequilibrium Surface Chemistry," 44th AIAA Thermophysics Conference, 2013. https://doi.org/10.2514/6.2013-2634.
- [4] Farbar, E. D., Alkandry, H., Wiebenga, J., and Boyd, I. D., "Simulation of Ablating Hypersonic Vehicles with Finite-Rate Surface Chemistry," 11th AIAA/ASME Joint Thermophysics and Heat Transfer Conference, 2014. https://doi.org/10.2514/6.2014-2124.
- [5] Candler, G. V., Johnson, H. B., Nompelis, I., Subbareddy, P. K., Drayna, T. W., Gidzak, V., and Barnhardt, M. D., "Development of the US3D Code for Advanced Compressible and Reacting Flow Simulations," 53rd AIAA Aerospace Sciences Meeting, 2015.
- [6] McQuaid, J. A., Zibitsker, A. L., Martin, A., and Brehm, C., "Simulation of Graphite Ablation Using an Overset Near Body Solver on an Adaptative Block-structured Cartesian Off-body Grid," AIAA Aviation Forum, 2022. https://doi.org/10.2514/6.2022-4088.
- [7] Zibitsker, A. L., Martin, A., McQuaid, J. A., Brehm, C., Palmer, G., Libben, B., and Stern, E., "Study of Graphite Ablation at Arc-Jet Conditions using Finite-Rate and Equilibrium Chemistry Models," 11th International Conference on Computational Fluid Dynamics, 2022.
- [8] Loridan, V., Peluchon, S., and Claudel, J., "Investigating the accuracy of a fully coupled fluid / thermal strategy with nonequilibrium chemistry to compute graphite ablation," AIAA AVIATION 2023 Forum, 2023. https://doi.org/10.2514/6.2023-3329.
- [9] Scoggins, J. B., Leroy, V., Bellas-Chatzigeorgis, G., Dias, B., and Magin, T. E., "Mutation++: MUlticomponent Thermodynamic And Transport properties for IONized gases in C++," SoftwareX, Vol. 12, 2020, p. 100575. https://doi.org/https://doi.org/10.1016/j.softx.2020.100575.
- [10] Novello, P., Poëtte, G., Lugato, D., Peluchon, S., and Congedo, P. M., "Accelerating hypersonic reentry simulations using deep learning-based hybridization (with guarantees)," *Journal of Computational Physics*, Vol. 498, 2024, p. 112700. https://doi.org/https://doi.org/10.1016/j.jcp.2023.112700.
- [11] Wilke, C. R., "A Viscosity Equation for Gas Mixtures," *The Journal of Chemical Physics*, Vol. 18, No. 4, 1950, pp. 517–519. https://doi.org/10.1063/1.1747673.

- [12] Blottner, F. G., Johnson, M., and Ellis, M., "Chemically Reacting Viscous Flow Program For Multi-Component Gas Mixtures," 1971. https://doi.org/10.2172/4658539.
- [13] Martin, A., Zhang, H., and Tagavi, K. A., "An Introduction to the Derivation of Surface Balance Equations Without the Excruciating Pain," *International Journal of Heat and Mass Transfer*, Vol. 115, 2017, pp. 992–999. https://doi.org/https://doi.org/10.1016/j.ijheatmasstransfer.2017.07.078.
- [14] Park, C., "Review of chemical-kinetic problems of future NASA missions. I Earth entries," *Journal of Thermophysics and Heat Transfer*, Vol. 7, No. 3, 1993, pp. 385–398. https://doi.org/10.2514/3.431.
- [15] Park, C., Jaffe, R. L., and Partridge, H., "Chemical-Kinetic Parameters of Hyperbolic Earth Entry," Journal of Thermophysics and Heat Transfer, Vol. 15, No. 1, 2001, pp. 76–90. https://doi.org/10. 2514/2.6582.
- [16] Havstad, M. A., and Ferencz, R. M., "Comparison of Surface Chemical Kinetic Models for Ablative Reentry of Graphite," *Journal of Thermophysics and Heat Transfer*, Vol. 16, No. 4, 2002, pp. 508–515. https://doi.org/10.2514/2.6725.
- [17] Candler, G., "Nonequilibrium Processes in Hypervelocity Flows: An Analysis of Carbon Ablation Models," 50th AIAA Aerospace Sciences Meeting including the New Horizons Forum and Aerospace Exposition, 2012. https://doi.org/10.2514/6.2012-724.
- [18] Park, C., "Effects of Atomic Oxygen on Graphite Ablation," *AIAA Journal*, Vol. 14, No. 11, 1976, pp. 1640–1642. https://doi.org/10.2514/3.7267.
- [19] Park, C., "Stagnation-Point Ablation of Carbonaceous Flat Disks. I Theory," AIAA Journal, Vol. 21, No. 11, 1983, pp. 1588–1594. https://doi.org/10.2514/3.8293.
- [20] Park, C., "Calculation of Stagnation-Point Heating Rates Associated with Stardust Vehicle," Journal of Spacecraft and Rockets, Vol. 44, No. 1, 2007, pp. 24–32. https://doi.org/10.2514/1.15745.
- [21] Zhluktov, S. V., and Abe, T., "Viscous Shock-Layer Simulation of Airflow past Ablating Blunt Body with Carbon Surface," *Journal of Thermophysics and Heat Transfer*, Vol. 13, No. 1, 1999, pp. 50–59. https://doi.org/10.2514/2.6400.
- [22] Poovathingal, S., Schwartzentruber, T. E., Murray, V. J., Minton, T. K., and Candler, G. V., "Finite-Rate Oxidation Model for Carbon Surfaces from Molecular Beam Experiments," AIAA Journal, Vol. 55, No. 5, 2017, pp. 1644–1658. https://doi.org/10.2514/1.J055371.
- [23] Prata, K. S., Schwartzentruber, T. E., and Minton, T. K., "Air-Carbon Ablation Model for Hypersonic Flight from Molecular-Beam Data," AIAA Journal, Vol. 60, No. 2, 2022, pp. 627–640. https://doi.org/10.2514/1.J060516.
- [24] Baker, R. L., "Graphite Sublimation Chemistry Nonequilibrium Effects," AIAA Journal, Vol. 15, No. 10, 1977, pp. 1391–1397. https://doi.org/10.2514/3.60806.
- [25] Fagnani, A., Helber, B., Hubin, A., and Chazot, O., "3D Infrared Temperature Maps Measurements of Ablative Materials During Plasma Wind Tunnel Experiments," *Measurement Science and Technology*, Vol. 34, No. 7, 2023, p. 075401. https://doi.org/10.1088/1361-6501/acc67c.
- [26] Klauner, J., Henneaux, D., Schrooyen, P., Magin, T., and Chatelain, P., "High-Order Immersed Interface Framework To Model Graphite Ablation Subjected To High Enthalpy Facility," 3rd International Conference on Flight Vehicles, Aerothermodynamics and Re-entry, 2025.
- [27] Chen, Y.-K., Milos, F., Reda, D., and Stewart, D., "Graphite Ablation and Thermal Response Simulation Under Arc-Jet Flow Conditions," 36th AIAA Thermophysics Conference, 2003. https://doi.org/10.2514/6.2003-4042.
- [28] Chen, Y.-K., and Milos, F. S., "Navier-Stokes Solutions with Finite Rate Ablation for Planetary

- [29] Bianchi, D., Nasuti, F., and Martelli, E., "Navier-Stokes Simulations of Hypersonic Flows with Coupled Graphite Ablation," *Journal of Spacecraft and Rockets*, Vol. 47, No. 4, 2010, pp. 554–562. https://doi.org/10.2514/1.47995.
- [30] Bersbach, C. J., Evans, J., Alkandry, H., Ewing, M. E., and Isaac, D. A., "Ablative Thermal Response Numerical Modeling Under Arcjet Test Conditions," *Journal of Thermophysics and Heat Transfer*, Vol. 36, No. 3, 2022, pp. 627–636. https://doi.org/10.2514/1.T6346.
- [31] Gnoffo, P., and Johnston, C., "A Boundary Condition Relaxation Algorithm for Strongly Coupled, Ablating Flows including Shape Change," 42nd AIAA Thermophysics Conference, 2012. https://doi.org/10.2514/6.2011-3760.